

Interferometry by Deconvolution of Multicomponent Multioffset GPR Data

Evert Slob

Abstract—Interferometric techniques are now well known to retrieve data between two receivers by the cross correlation of the data recorded by these receivers. Cross-correlation methods for interferometry rely mostly on the assumption that the medium is loss free and that the sources are all around the receivers. A recently developed method introduced interferometry by deconvolution that is insensitive to loss mechanisms by principle and requires sources only on one side of the receivers. In this paper, we develop such method for ground-penetrating radar, illustrate the concept, and discuss implications for practical applications with numerical examples.

Index Terms—Deconvolution, ground-penetrating radar (GPR) data, interferometry, multicomponent, multioffset.

I. INTRODUCTION

THE NOTION of interferometry to mean the generation of pulse-echo responses from passive recordings and to use the newly constructed data for imaging the surroundings is known for more than 20 years [1], [2]. During the last eight years, many interferometric methods have been developed for random fields and for controlled-source data. What the underlying theories have in common is that the medium is assumed to be lossless and reciprocal. The main reason for this underlying assumption is that the wave equation in lossless and reciprocal media is invariant for time reversal. For an overview of the theory of “seismic interferometry” or “Green’s function retrieval” and its applications to passive as well as controlled-source data, we refer to a reprint book [3], which contains a large number of papers on this subject. Similarly, time-reversal techniques are well known in several branches of science and technology, and they are still actively being researched [4]–[9]. Model-driven time-reversal imaging techniques can account for energy dissipation by not only correcting for travel time delay but also for amplitude effects [10].

The first analysis of the interferometric method for ground-penetrating radar (GPR) data, in which losses play a prominent role, can be found in [11]. It was shown that losses lead to amplitude errors as well as the occurrence of spurious events. By choosing the recording locations in a specific way,

the spurious events arrive before the first desired arrival and can thus be identified [12]. In many applications in natural soil, the losses are too high to neglect, and this problem can be circumvented using cross-convolution techniques when the sources are located on an irregular boundary [13]. The number of acquisition configurations where cross-convolution methods can be used is rather limited. By choosing one receiver in a lossless medium, e.g., air, and a configuration with all dissipative parameters outside the surface distribution of noise or transient sources, cross-correlation methods work without strong amplitude errors in the time window of interest [14]. A cross-borehole application of the cross-correlation method can be found in [15]. The occurrence of spurious events decreases with increasing irregularity of the boundary surface and decreases with increasing strength of the subsurface heterogeneity. This approach is valid for waves and diffusive fields in dissipative media. Independently, it was shown that a volume distribution of uncorrelated noise sources, with source strengths proportional to the dissipation parameters of the medium, precisely compensates for the energy losses [16]–[18]. As a consequence, the responses obtained by interferometry in such configurations are error free. Also, this approach holds for waves in dissipative media and for pure diffusion processes. Recently, it was shown that interferometry by cross correlation, including its extensions for waves and diffusion in dissipative and/or moving media, can be represented in a unified form [19], [20]. From the results of these studies, we conclude that the previously described methods provide a rather limited practical approach to applications where intrinsic loss factors play a significant role. For specific configurations, interferometry can be applied through a deconvolution of the up going field by the down going field at the same depth level [21]. Here, we demonstrate that “interferometry by deconvolution (IbD)” is suitable for GPR applications.

II. ONE-DIMENSIONAL RADAR WAVE INTERFEROMETRY IN DISSIPATIVE MEDIA

Let us start by illustrating the concept in a 1-D setting. The 1-D version of IbD was introduced by Riley and Claerbout for seismic waves [22]. It is valid for dissipating media, and therefore, it is of interest for GPR applications. It starts with a source in a stack of layers, and the fields that define the energy state are recorded at a particular depth level away from the source level. These recorded fields can be decomposed into flux-normalized down and up going wave field potentials. At any source-free depth level z_l and for any frequency value ω , we can write the electric $\hat{E}(z_l, \omega)$ and magnetic $\hat{H}(z_l, \omega)$ fields

Manuscript received July 1, 2008; revised August 20, 2008. First published February 3, 2009; current version published February 19, 2009. This work was supported by the Netherlands Research Centre for Integrated Solid Earth Science.

The author is with the Department of Geotechnology, Delft University of Technology, 2628 Delft, The Netherlands (e-mail: E.C.Slob@TUDelft.NL).

Color versions of one or more of the figures in this paper are available online at <http://ieeexplore.ieee.org>.

Digital Object Identifier 10.1109/TGRS.2008.2005250

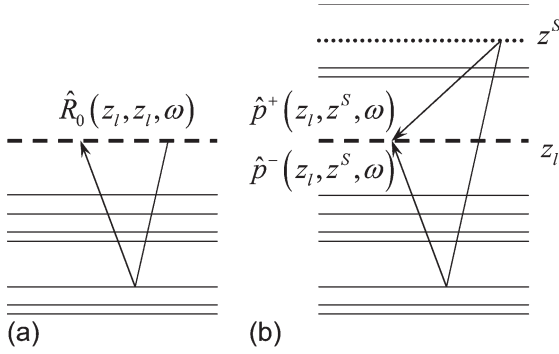


Fig. 1. (a) The response of the medium below z_l with a homogeneous upper half-space above z_l . (b) The measured response of the real earth.

in terms of up going $\hat{p}^-(z_l, \omega)$ and down going $\hat{p}^+(z_l, \omega)$ wave field potentials as

$$\begin{bmatrix} \hat{E}(z_l, \omega) \\ \hat{H}(z_l, \omega) \end{bmatrix} = \frac{1}{\sqrt{2}} \begin{bmatrix} \sqrt{\hat{Z}(\omega)} & \sqrt{\hat{Z}(\omega)} \\ \sqrt{\hat{Y}(\omega)} & -\sqrt{\hat{Y}(\omega)} \end{bmatrix} \begin{bmatrix} \hat{p}^+(z_l, \omega) \\ \hat{p}^-(z_l, \omega) \end{bmatrix} \quad (1)$$

where, for the moment, we assume that the medium parameters are continuous across the depth level z_l . The plane wave impedance \hat{Z} is given by $\hat{Z} = \sqrt{\zeta/\eta}$, with $\zeta = j\omega\mu$, μ being the magnetic permeability, and $\eta = j\omega\hat{\epsilon} + \hat{\sigma}$, where the electric permittivity and conductivity are given by $\hat{\epsilon}$ and $\hat{\sigma}$. The plane wave admittance \hat{Y} is the reciprocal of the plane wave impedance. We call the up and down going wave field potential flux normalized because the unit of these decomposed wave fields $\hat{p}^\pm(z_l, \omega)$ in the space-time domain is \sqrt{J}/m . For a source located above the receiver level, it was shown that the up going part deconvolved in the time domain by the down going part yields the reflection response of the stack of layers that are below the receivers, while all other interfaces have disappeared and a homogeneous half-space exists above the receiver level. Deconvolution in the time domain corresponds in the frequency domain to division, which can be written as

$$\hat{R}_0(z_l, z_l, \omega) = \hat{p}^-(z_l, z^S, \omega) / \hat{p}^+(z_l, z^S, \omega) \quad (2)$$

where $\hat{R}_0(z_l, z_l, \omega)$ denotes the unitless reflection response of the layered earth that is homogeneous above the receiver level z_l , which is now also the source level. Using (1), we can also write (2) directly in terms of the measured electric and magnetic field strengths

$$\hat{R}_0(z_l, z_l, \omega) = \frac{\sqrt{\hat{Y}(\omega)}\hat{E}(z_l, z^S, \omega) - \sqrt{\hat{Z}(\omega)}\hat{H}(z_l, z^S, \omega)}{\sqrt{\hat{Y}(\omega)}\hat{E}(z_l, z^S, \omega) + \sqrt{\hat{Z}(\omega)}\hat{H}(z_l, z^S, \omega)} \quad (3)$$

The source location z^S is now put explicitly in the expressions for the up going wave field $\hat{p}^-(z_l, z^S, \omega)$ and down going wave field $\hat{p}^+(z_l, z^S, \omega)$, which are again flux-normalized recorded wave field potentials in the measurement configuration with heterogeneities below and above the source and receiver levels. This is shown in Fig. 1 where the right graph shows the measurement configuration with reflectors above and below the source and receivers, and the left graph shows the result after

division in the frequency domain. In the right-hand side of (2), two recorded wave fields occur, the up going field at the receiver level and the down going field at the receiver level, both due to a source at a higher level. In the left-hand side of (2), a reflection response occurs at the receiver level due to a source at that same level. We have hereby created a new response through deconvolution that can be understood as a weighted form of cross correlation, for which reason we call it IbD [23]. A straight division as described in (2) can be numerically unstable, and a stabilized version is given by

$$\hat{R}_0(z_l, z_l, \omega) = \frac{\hat{p}^-(z_l, z^S, \omega) [\hat{p}^+(z_l, z^S, \omega)]^*}{|\hat{p}^+(z_l, z^S, \omega)|^2 + \epsilon^2} \quad (4)$$

where the superscript * denotes complex conjugation and ϵ is the stabilization factor. The following two important observations can be made from (2) and Fig. 1. First, we have eliminated the original source without needing to know its location other than that it must be located above the receiver level. Second, this newly created response does not contain the direct field, which is usually strong in GPR applications, nor does it contain any information from the level above the receivers. The method is called data driven because the measured electric and magnetic field strengths are used to construct the reflection response. In the decomposition step, the medium parameters must be known, and this is the only non-data-driven part, although the expected absence of the direct field in the reflection response can be used as a criterion to estimate these medium parameters from the data as well.

Consequentially, above surface objects, whose presence show up as reflections that can hamper GPR data interpretation [24], [25], are eliminated in this process. Eliminating the overburden can be achieved through IbD at any depth level. This implies that it is very suitable in monitoring studies when a horizontal borehole is available, and the changes in the target zone can be studied using time-lapse GPR data, without being bothered by all changes in the subsurface above the target zone, e.g., changed weather conditions or changes due to anthropogenic activities. A last interesting detail in this procedure, which was not considered in [22], is the possible presence of an interface at the receiver level, such as the Earth surface. Fig. 1 is just a sketch, and the exact location of the up and down going wave fields is not specified. If the receivers are located in a homogeneous layer, the up going wave field just above the receiver level is the same as the up going wave field just below the receiver level, and the same applies for the down going wave fields. However, although the recorded transverse electric and magnetic field components are continuous across an interface, the decomposed wave field potentials are not. This implies that when the receivers are located at an interface between two different layers, different up and down going wave field potentials occur at both sides of the interface as shown in Fig. 2 and both can be recovered. In principle, it does not matter whether the up and down going field potentials above or below the interface are used. Of course, the presence of the interface remains in the created data when the up and down going wave field potentials above the interface are used, while it vanishes when the up and down going wave field potentials

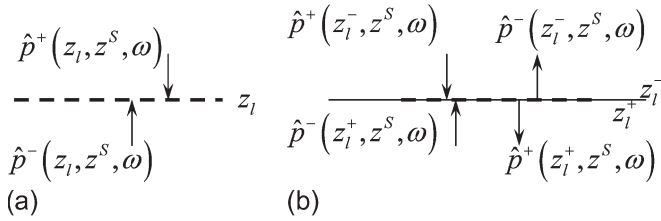


Fig. 2. (a) Receivers at a homogeneous level. Up going waves only come from below the receiver level, while down going waves only come from above the receiver level. (b) Receiver at an interface of discontinuity. Up and down going waves occur at both sides of the receiver level.

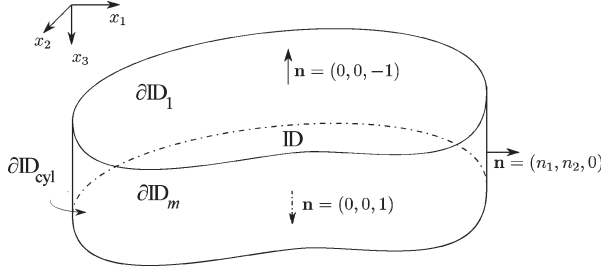


Fig. 3. Configuration for one-way reciprocity theorems.

below the interface are used. In particular, the Earth surface is usually a strong reflector, and for data recorded at the Earth surface, it is worthwhile to use the fields below the surface in the deconvolution. To carry out the decomposition of the data into up and down going wave field potentials below the Earth surface, it is necessary that the medium parameters just below the surface are known. They can be obtained by independent measurements or estimated from the data.

III. THREE-DIMENSIONAL RADAR WAVE INTERFEROMETRY IN DISSIPATIVE MEDIA

To facilitate such decomposition in a general 3-D heterogeneous setting, we employ the reciprocity theorem for one-way fields and apply it on a domain with two horizontal boundaries, see Fig. 3, and assume that the side of the domain is at infinity. The necessity of flat horizontal boundaries can be relaxed under certain conditions, and the derived representations also hold for smoothly curved boundaries [26]. Following [27], we write the frequency domain one-way field reciprocity theorem for two independent states A and B as

$$\int_{\partial\mathbb{D}} n_3 (\hat{\mathbf{p}}_A)^t \mathbf{N} \hat{\mathbf{p}}_B d^2 \mathbf{x} = \int_{\mathbb{D}} \{ (\hat{\mathbf{p}}_A)^t \mathbf{N} \hat{\mathbf{s}}_B + (\hat{\mathbf{s}}_A)^t \mathbf{N} \hat{\mathbf{p}}_B \} d^3 \mathbf{x} \quad (5)$$

where $\partial\mathbb{D}$ denotes the two flat boundaries with outward unit normal n_3 and the superscript t denotes transposition. The 4×1 electromagnetic one-way wave field vector \mathbf{p} contains flux-normalized down and up going fields $\hat{\mathbf{p}} = (\hat{\mathbf{p}}^+, \hat{\mathbf{p}}^-)^t$, and the 4×1 electromagnetic source vector contains flux-normalized down and up going source components $\hat{\mathbf{s}} = (\hat{\mathbf{s}}^+, \hat{\mathbf{s}}^-)^t$ given by the 2×1 vectors $\hat{\mathbf{p}}^\pm = \hat{\mathbf{p}}^\pm(\mathbf{x}, \omega)$ and $\hat{\mathbf{s}}^\pm = \hat{\mathbf{s}}^\pm(\mathbf{x}, \omega)$ [28]. The matrix \mathbf{N} is given by

$$\mathbf{N} = \begin{pmatrix} \mathbf{0} & \mathbf{I} \\ -\mathbf{I} & \mathbf{0} \end{pmatrix} \quad (6)$$

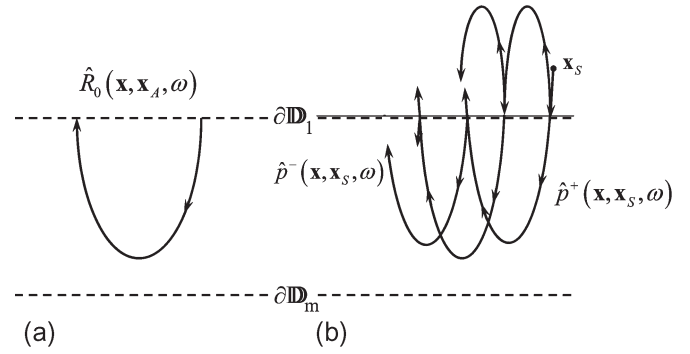


Fig. 4. (a) State A : The response of the medium inside \mathbb{D} with a homogeneous upper half-space above $\partial\mathbb{D}_1$. (b) State B : The measured response of the real earth. Both states have a homogeneous lower half-space below $\partial\mathbb{D}_m$.

where the matrices \mathbf{I} and $\mathbf{0}$ are the 2×2 identity and null matrices, respectively. To construct the vector $\hat{\mathbf{p}}$, we must record all horizontal components of the electric and magnetic field strengths on a grid, and we apply decomposition to these components. Note that (5) holds for equal media in the two states inside \mathbb{D} , while outside \mathbb{D} , the media in the two states can be different. The explicit expressions for the decomposition and composition operators are given in the Appendix. It suffices here to say that this decomposition can be carried out if the vertical component of the Poynting vector is known, which implies that the two horizontal components of the electric and magnetic field strengths are known. Electric field strengths are usually measured by GPR antennas, but also, small loop antennas can be used to measure the electromotive force that is directly related to the magnetic field [29], [30].

First, we assume that, in both states, the sources are outside \mathbb{D} ; this reduces (5) to

$$\int_{\partial\mathbb{D}_1} \{ (\hat{\mathbf{p}}_A^+)^t \hat{\mathbf{p}}_B^- - (\hat{\mathbf{p}}_A^-)^t \hat{\mathbf{p}}_B^+ \} d^2 \mathbf{x} = \int_{\partial\mathbb{D}_m} \{ (\hat{\mathbf{p}}_A^+)^t \hat{\mathbf{p}}_B^- - (\hat{\mathbf{p}}_A^-)^t \hat{\mathbf{p}}_B^+ \} d^2 \mathbf{x}. \quad (7)$$

In the following analysis, state A represents the desired reflection response with a new source at the receiver level of state B in an earth with different boundary conditions than the real earth, obtained through IbD. The difference is that the medium above the boundary $\partial\mathbb{D}_1$ is homogeneous and has the same properties as that just below $\partial\mathbb{D}_1$, see Fig. 4(a). For state A , we choose a down going source component just above the level $\partial\mathbb{D}_1$ and put receivers at the same level $\partial\mathbb{D}_1$. We define the reflection response of the medium below $\partial\mathbb{D}_1$ as the 2×2 matrix $\hat{\mathbf{R}}_0^+(\mathbf{x}, \mathbf{x}_A, \omega)$, where the subscript “0” denotes that no reflectors exist above the level $\partial\mathbb{D}_1$ and the superscript “+” indicates that the reflection is a response to a down going source field. We therefore find in state A for $\mathbf{x} \in \partial\mathbb{D}_1$

$$\begin{cases} \hat{\mathbf{p}}_A^+(\mathbf{x}, \omega) = \begin{pmatrix} \delta(\mathbf{x}_H - \mathbf{x}_{H,A}) & 0 \\ 0 & \delta(\mathbf{x}_H - \mathbf{x}_{H,A}) \end{pmatrix} \\ \hat{\mathbf{p}}_A^-(\mathbf{x}, \omega) = \hat{\mathbf{R}}_0^+(\mathbf{x}, \mathbf{x}_A, \omega) \end{cases} \quad (8)$$

where the subscript H is used to denote the horizontal coordinates only; hence, $\mathbf{x}_H = (x_1, x_2)$ and $\mathbf{x}_{H,A} = (x_{1,A}, x_{2,A})$,

the latter representing the horizontal coordinates of \mathbf{x}_A . At $\mathbf{x} \in \partial\mathbb{D}_m$, we have again only down going fields

$$\mathbf{x} \in \partial\mathbb{D}_m \quad \begin{cases} \hat{\mathbf{p}}_A^+(\mathbf{x}, \omega) = \hat{\mathbf{T}}^+(\mathbf{x}, \mathbf{x}_A, \omega) \\ \hat{\mathbf{p}}_A^-(\mathbf{x}, \omega) = \mathbf{0} \end{cases} \quad (9)$$

where $\hat{\mathbf{T}}^+(\mathbf{x}, \mathbf{x}_A, \omega)$ is the 2×2 transmission response between the levels $\partial\mathbb{D}_1$ and $\partial\mathbb{D}_m$.

State B represents the actual state of the measured response of the real earth. Consider the GPR acquisition geometry with an air-launched transmitter antenna, see Fig. 4, with a source at \mathbf{x}_S in the air and the receivers \mathbf{x} at the Earth surface $\partial\mathbb{D}_1$. Both in the air above the receiver antennas and below the receiver antennas in the domain between $\partial\mathbb{D}_1$ and $\partial\mathbb{D}_m$, there can be heterogeneities, and the medium can be dissipative anywhere in space. From (8), we can see that we would like to reconstruct a 2×2 reflection response matrix at each receiver location. This requires two source types, or two independent vector components, at each location. For each source component and after decomposition, we have for state B the down and up going components of the recorded earth response, including possible above surface reflections, given by

$$\mathbf{x} \in \partial\mathbb{D}_1 = \begin{cases} \hat{\mathbf{p}}_B^+(\mathbf{x}, \omega) = \hat{\mathbf{p}}^+(\mathbf{x}, \mathbf{x}_S, \omega) \\ \hat{\mathbf{p}}_B^-(\mathbf{x}, \omega) = \hat{\mathbf{p}}^-(\mathbf{x}, \mathbf{x}_S, \omega) \end{cases} \quad (10)$$

We choose the level $\partial\mathbb{D}_m$ to be below all heterogeneities; hence, there are only nonzero down going field components at the level $\partial\mathbb{D}_m$

$$\mathbf{x} \in \partial\mathbb{D}_m = \begin{cases} \hat{\mathbf{p}}_B^+(\mathbf{x}, \omega) = \hat{\mathbf{p}}^+(\mathbf{x}, \mathbf{x}_S, \omega) \\ \hat{\mathbf{p}}_B^-(\mathbf{x}, \omega) = \mathbf{0} \end{cases} \quad (11)$$

These two vectors for the up and down going fields for each source type or component are put in 2×2 matrices $\hat{\mathbf{P}}^\pm(\mathbf{x}, \omega)$ given by

$$\mathbf{x} \in \partial\mathbb{D}_1 \quad \begin{cases} \hat{\mathbf{P}}_B^+(\mathbf{x}, \omega) = \hat{\mathbf{P}}^+(\mathbf{x}, \mathbf{x}_S, \omega) \\ \hat{\mathbf{P}}_B^-(\mathbf{x}, \omega) = \hat{\mathbf{P}}^-(\mathbf{x}, \mathbf{x}_S, \omega) \end{cases} \quad (12)$$

$$\mathbf{x} \in \partial\mathbb{D}_m \quad \begin{cases} \hat{\mathbf{P}}_B^+(\mathbf{x}, \omega) = \hat{\mathbf{P}}^+(\mathbf{x}, \mathbf{x}_S, \omega) \\ \hat{\mathbf{P}}_B^-(\mathbf{x}, \omega) = \mathbf{0} \end{cases} \quad (13)$$

The substitution of (8) and (9), (12) and (13) into (7) and using source–receiver reciprocity, i.e., $\hat{\mathbf{R}}_0^+(\mathbf{x}, \mathbf{x}_A, \omega) = (\hat{\mathbf{R}}_0^+)^t(\mathbf{x}_A, \mathbf{x}, \omega)$ yields

$$\hat{\mathbf{P}}^-(\mathbf{x}_A, \mathbf{x}_S, \omega) = \int_{\mathbf{x} \in \partial\mathbb{D}_1} \hat{\mathbf{R}}_0^+(\mathbf{x}_A, \mathbf{x}, \omega) \hat{\mathbf{P}}^+(\mathbf{x}, \mathbf{x}_S, \omega) d^2\mathbf{x}. \quad (14)$$

Equation (14) is a Fredholm integral equation of the first kind in the reflection response matrix $\hat{\mathbf{R}}_0^+(\mathbf{x}_A, \mathbf{x}, \omega)$. The reflection response matrix is the retrievable flux-normalized Green's function, representing the impulse response at a receiver location $\mathbf{x}_A \in \partial\mathbb{D}_1$ due to a down going source component at position $\mathbf{x} \in \partial\mathbb{D}_1$. For laterally invariant media, it can easily be solved by a simple 2×2 matrix inversion for each wavenumber–frequency component separately. Of course, this requires two independent source components. For general 3-D

heterogeneous media, it can only be solved when the decomposed data $\hat{\mathbf{P}}^-(\mathbf{x}_A, \mathbf{x}_S, \omega)$ and $\hat{\mathbf{P}}^+(\mathbf{x}, \mathbf{x}_S, \omega)$ are recorded at a sufficient number of receiver positions $\mathbf{x}_A \in \partial\mathbb{D}_1$ and for a sufficient number of source positions \mathbf{x}_S . It follows that two horizontal source electric dipole orientations are sufficient to solve (14), see, e.g., [31] for an elastic example. In matrix notation [32], (14) can be written as

$$\hat{\mathbf{P}}^- = \hat{\mathbf{R}}_0^+ \hat{\mathbf{P}}^+. \quad (15)$$

For example, the columns of matrix $\hat{\mathbf{P}}^+$ contain both components of $\hat{\mathbf{p}}^+(\mathbf{x}, \mathbf{x}_S, \omega)$ for fixed \mathbf{x}_S and variable \mathbf{x} at $\partial\mathbb{D}_1$, whereas the rows of this matrix contain $\hat{\mathbf{p}}^+(\mathbf{x}, \mathbf{x}_S, \omega)$ for fixed \mathbf{x} and variable \mathbf{x}_S and both source components at $\partial\mathbb{D}_S$, where $\partial\mathbb{D}_S$ represents the depth level of the sources. The inversion of (15) involves matrix inversion in some generalized sense. Since the number of source positions is not necessarily equal to the number of receiver positions, (15) does not necessarily constitute a square problem. We can write the formal solution as [33]

$$\hat{\mathbf{R}}_0^+ = \hat{\mathbf{P}}^-(\hat{\mathbf{P}}^+)^{-1}. \quad (16)$$

An explicit expression for the reflection response in terms of the electric and magnetic field strengths, analogous to (3), is given in the Appendix. The matrix inversion in (16) can be solved in the least squares sense using a stabilized form given by

$$\hat{\mathbf{R}}_0^{+, \text{IbD}} = \hat{\mathbf{P}}^-(\hat{\mathbf{P}}^+)^{\dagger} \left[\hat{\mathbf{P}}^+(\hat{\mathbf{P}}^+)^{\dagger} + \epsilon^2 \mathbf{I} \right]^{-1} \quad (17)$$

where the superscript \dagger denotes transposition and complex conjugation, \mathbf{I} is the identity matrix, and ϵ is a small constant. This method automatically deconvolves for the time source signature, and the impulse response is obtained. A similar inversion is used for transforming acoustic surface-related multiples into primaries [34]. Equations (16) and (17) describe 3-D IbD and are similar to the least squares redatuming method [35]. When we ignore the inverse matrix in (17), we arrive at

$$\hat{\mathbf{R}}_0^{+, \text{CC}} \approx \hat{\mathbf{P}}^-(\hat{\mathbf{P}}^+)^{\dagger} |\hat{S}|^{-2} \quad (18)$$

which is the matrix form expression in the frequency domain and is similar to the scalar acoustic virtual source method [36]. The factor $|\hat{S}|^2$ denotes the power spectrum of the source signature because the autocorrelation of the time source signature is in the numerator and must be compensated for. This implies that, when this approach is used on measured data, this power spectrum should be known. Of course, in general, the matrix $\hat{\mathbf{P}}^+(\hat{\mathbf{P}}^+)^{\dagger}$ is not close to \mathbf{I} , and (18) cannot be used for most GPR data. In the time domain, this matrix inversion is equivalent to space-time deconvolution with the autocorrelation of the down going field potential. This autocorrelation obviously has its major component in the origin, which would amount to merely a scaling amplitude factor. However, the autocorrelation also contains all interactions with the first down going wave and all later arrivals, which remain in the autocorrelation at times different than zero. These events eliminate all events related to the medium above the receivers that are present in the up going

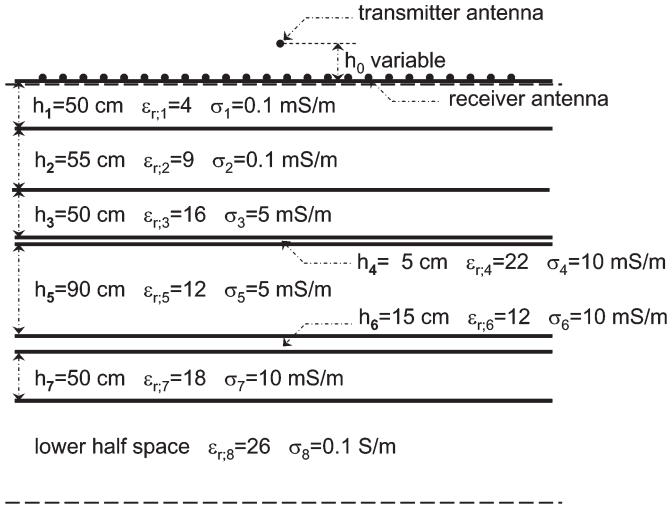


Fig. 5. Model configuration for the numerical examples. The transmitting antenna is located in the air above a model with seven layers of finite thickness, and the receiving antennas are located on the surface allowing for decomposition just above or just below the surface, indicated by the dashed line.

wave field potential. When the reflectors above the receivers are weak and/or far away from the reflectors below the receivers, they can be neglected, and then, the cross-correlation method of (18) will produce accurate results. When the stabilization factor ϵ^2 is taken very large, IbD becomes a scaled version of CC. When the factor becomes very small, the noise in the data and the evanescent waves will blow up and destroy the result. Hence, ϵ^2 should be taken as small as possible but large enough to prevent blow up of unwanted features. The two possible methods to reconstruct a reflection response are illustrated with two numerical examples.

IV. NUMERICAL EXAMPLES

A 1-D layered earth is used to illustrate the concept and discuss some implications for practical applications of the developed method in this paper. The configuration is shown in Fig. 5, where the electric permittivity and conductivity of a layered half-space below the surface with seven layers of finite thickness and different permittivity conductivity values are indicated in the layers. The magnetic permeability of all layers in the model has the free space value. For the first example, the source height h_0 is 24 cm above the surface, and the source time signature is a Ricker wavelet with a center frequency of 250 MHz. The wave field is modeled with parallel y -directed antennas of infinite length and with an offset in the x -direction, as a 2-D model for the regular surface reflection GPR parallel broadside setup. The receivers are placed on the surface. In addition, the x -directed magnetic field component is modeled and used for the up-down wave field separation. Because the layered model is 1-D, we can carry out the up-down wave field separation in the wavenumber-frequency domain, and the matrix inversion described in (17) is replaced by a multidimensional deconvolution, which can also be carried out in the wavenumber-frequency domain by pointwise division. This implementation is equivalent to using the same offsets for sources and receivers, and it was taken as 10 cm

in the computation of the presented examples. The recorded y -component of the electric field is shown in Fig. 6 in both wavenumber-frequency (a) and space-time (b) domains. The color axis in Fig. 6(a) is chosen such that all amplitudes below -90 dB relative to the maximum amplitude are saturated blue and the horizontal axis is a function of wavenumber. For all wavenumber-frequency plots, we use the wavenumber $\lambda = k/(2\pi)$ and frequency $f = \omega/(2\pi)$. In Fig. 6(a), two straight lines can be seen; across which, strong amplitude changes occur. These are the lines corresponding to $f/\lambda = c_0$ and $f/\lambda = c_1$, which correspond to the direct air and ground waves, respectively. The color axis in Fig. 6(b) is chosen such that all strengths above 10% of the maximum are saturated red and below 10% of the minimum are saturated blue to ensure visibility of weaker reflections at later times. The up-down separation is carried out using the y -component of the electric field and the x -component of the magnetic field according to the 2-D equivalent of (34). To circumvent reconstruction of numerical accuracy, the stabilization value was chosen to be

$$\epsilon^2 = 10^{-4.5} \times \max\{\hat{P}^+(\hat{P}^+)^{\dagger}\} \quad (19)$$

such that all numbers below the -45 -dB point are saturated for computing the inverse expression between the square brackets in the right-hand side of (17). The inversion procedure of (17) with the defined value for ϵ^2 and the cross-correlation procedure of (18) is carried out in the wavenumber domain, and the amplitude of the result is shown in decibels after normalizing the amplitude to the maximum of the down going wave field amplitude. The results are shown in Fig. 7 for the IbD in wavenumber-frequency (a) and space-time (b) domains, and for interferometry by cross correlation in wavenumber-frequency and space-time domains in Fig. 7(c) and (d), respectively. By comparing the spectra in Fig. 7(a) and (c), it can be seen that information about the air layer is still in the cross-correlation result, while it has disappeared in the IbD result. With this value of ϵ^2 , the full reflection response is reconstructed, and the wavenumber-frequency plot of the direct modeled reflection response is indistinguishable from the reflection response reconstructed with IbD. This can be expected because the reconstructed spectrum is well within the -45 -dB level of the recorded data. The reason is that the original source height is relatively small compared to the dominant wavelength of the source signature. Hence, in the space-time domain, the result in Fig. 7(b) corresponds to the exact reflection response, which is the same as the result obtained by IbD. This shows the full potential of the method when the bandwidth of the data is sufficiently wide for the construction of the reflection response. The CC result shown in Fig. 7(d) shows that, although the main features are all present, a lot of artifacts can be observed due to the fact that the surface-related events have not been eliminated. This elimination is only achieved by matrix inversion. A more difficult configuration is when the sources are lifted higher above the ground surface. If the height is increased such that antennas are in the far field, the effect of spectrum masking is visible. The height is increased to 10 m above the ground surface, and the wavenumber-frequency and space-time domain plots are shown in Fig. 8. Because the

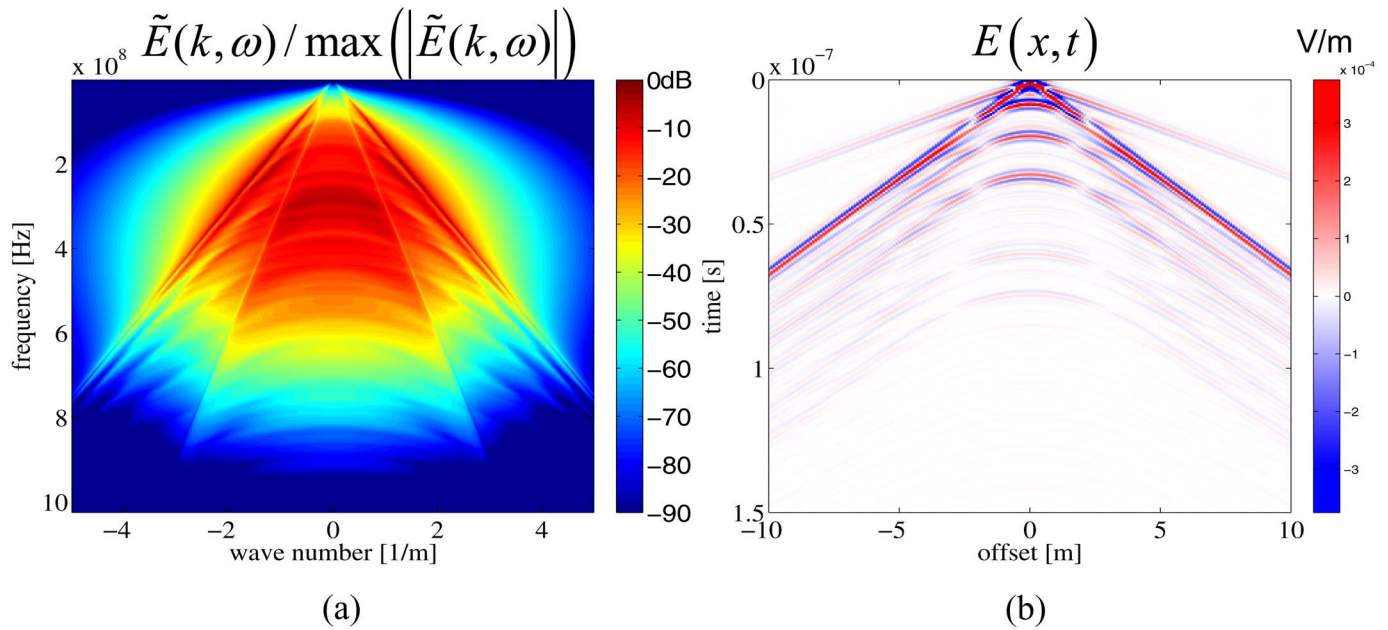


Fig. 6. (a) Wavenumber–frequency and (b) space-time plots of the electric field recording of receivers for the configuration in Fig. 5 with one transmitter antenna position at $h_0 = 24$ cm above the ground surface.

spatial bandwidth is now rather limited, we can take a 25-cm spacing between the receivers to avoid aliasing, and the maximum offset is comparably enlarged. From the spectrum in Fig. 8(a), it can be seen that the line $\lambda = f/c_0$ is the cut-off line, and for all wavenumbers $\lambda > f/c_0$, the waves are evanescent and are exponentially damped very strongly due to the large vertical distance between the ground surface and the transmitter antenna. This loss of information cannot be retrieved by any data processing method. The up–down wave field decomposition can still be carried out within the available bandwidth, and the IbD and cross correlation are carried out to obtain a spectrum within the bandwidth of the original data. These wavenumber–frequency domain results, scaled by the maximum amplitude of the electric field of Fig. 8(a), are shown in Fig. 9(a) for IbD and in Fig. 9(c) for cross correlation. The corresponding space-time domain results are shown in Fig. 9(b) and (d). These results should be compared with Fig. 7(a) and (b) where the exact results as obtained by IbD are shown in wavenumber–frequency domain (scaled by a different factor) and in space-time domain. It can be concluded that the wavenumber domain bandwidth is quite limited for this situation. This is exemplified in the space-time domain results where, in Fig. 9(b), the large offset slopes of all reflections run parallel and relate to the wave velocity in air. This is due to the fact that, below the surface, there is no wave energy propagating at angles beyond the critical angle due to the large vertical distance above the surface of the original source. Only in a limited offset range is the reflection response correctly retrieved, but even there, the effect of the limited bandwidth is visible by noncausal events that are extensions of the large offset events. In Fig. 9(d), it can be seen that, for early times, the reflection events look almost correct for short offsets, but at later times, many spurious events show up. These spurious events are caused by higher amplitude multiple surface interactions that

are present in the down going wave field potential, and these can be reduced by time windowing the down going wave field potential before carrying out the cross correlation. A second important observation is that the noncausal events that are strongly visible in the IbD results are much weaker in the CC result. The reason is that the amplitude in the wavenumber–frequency domain is much smaller in the CC result near wavenumbers that correspond to the free space wavenumber, as can be seen in Fig. 9(c), while in the IbD result, there is almost a step change in amplitude near those wavenumbers, as can be seen in Fig. 9(a). Hence, in the IbD results, they can be filtered out by filtering the wavenumber–frequency domain near the sudden change in amplitude (where one goes from propagating to evanescent waves). A geometrical interpretation would be that, for all incidence angles larger than 30° , no source energy is present in the reconstructed data. The IbD procedure eliminates the ground surface, and the upper half-space has the properties of the first layer. Then, with a source and receiver height of 50 cm above the first interface, the offset at which no propagating wave field is retrieved is 87 cm. This is shown in Fig. 10 where the zero and 1-m offset reconstructed A-scans are shown in (a) and (b), respectively. In this figure, all traces are normalized to their own maximum. The reason is that, in the cross-correlation method, the source wavelet is squared in amplitude, and to correct it, spectral balancing is required, which is easily done when the source wavelet is known. The second reason is that, in the cross-correlation method, the amplitude of the down going wave field is neglected. The zero offset results in Fig. 10(a) are quite good, although the cross-correlation result has a higher level of spurious events. As expected, the results at 1-m offset shown in Fig. 10(b) already suffer from strong amplitude effects, and spurious events emerge in the IbD results, while the cross-correlation result is almost no longer useful because a lot of multiple events remain in the data with strong amplitudes. To

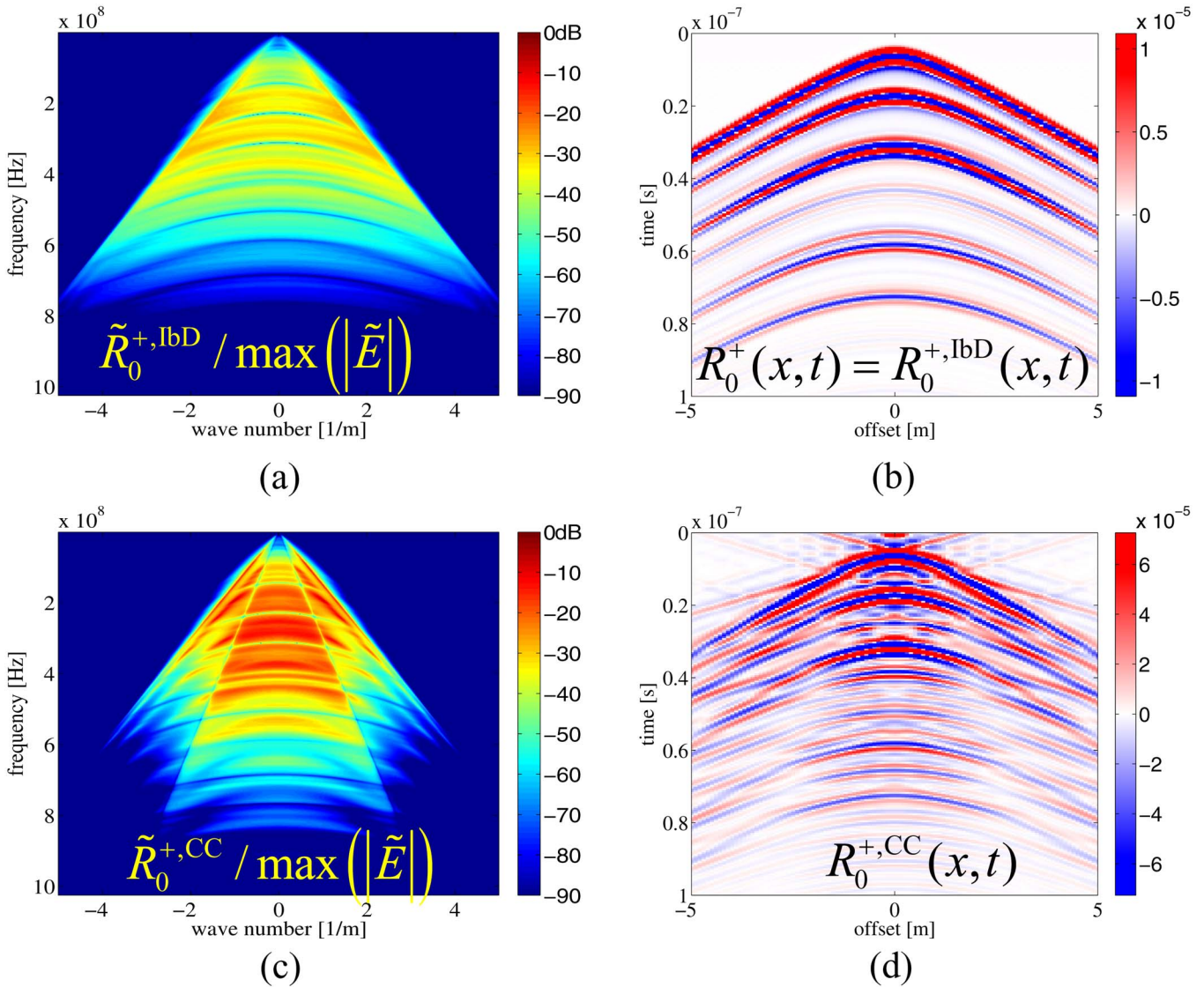


Fig. 7. Reflection responses obtained by IbD in the (a) wavenumber–frequency and (b) space–time domains and similar results obtained by cross correlation in the (c) wavenumber–frequency and (d) space–time domains. The wavenumber–frequency domain results are normalized by the maximum amplitude of the electric field strength.

demonstrate that the IbD results have quite accurate amplitudes at small offsets even though the bandwidth is quite limited, Fig. 11 shows the zero and 50-cm offset results in the true amplitude of the direct modeled trace, labeled as the exact result, and the result from the IbD procedure. At zero offset, Fig. 11(a), the first onset of the signal is overestimated in the reflections from the first two interfaces, while the other reflection events are retrieved with a high degree of accuracy. At a 50-cm offset, Fig. 11(b), the amplitude of the first reflection event is underestimated, but the others are all quite accurately retrieved. Deeper interfaces are obtained correctly for longer offsets because the travel paths still fall within the available bandwidth.

V. CONCLUSION

The concept of IbD has been illustrated, and the full 3-D form has been derived. The method effectively eliminates the sources

used in an experiment where the receivers are in a plane and all sources are located on one side of the receiver plane. The method replaces the heterogeneous medium above the receiver level by a half-space that has the medium parameters of the medium at the receiver level. It consists of two steps; first, the measured wave field is decomposed in up and down going wave fields using flux normalization in the decomposition. The second step is to resolve the reflection response matrix from a matrix equation that writes the up going wave field as the matrix product of the reflection response matrix and the down going wave field matrix. Only in the decomposition step is the information of the medium at the receiver level required; all other steps are completely data driven.

One example showed that, when the spectral information of the wave field that is to be reconstructed in the reflection response matrix is present in the recorded data, the IbD reconstruction is perfect. The second showed that one cannot retrieve more information than that present in the data. In particular, for

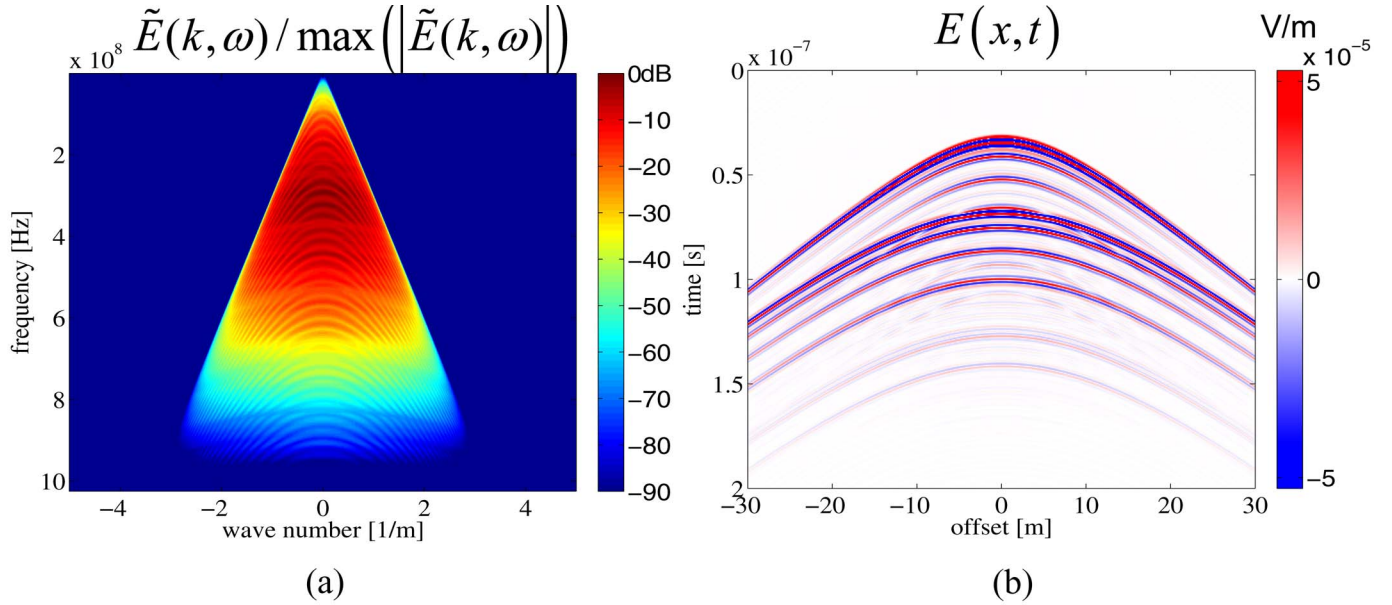


Fig. 8. (a) Wavenumber–frequency and (b) space-time plots of the electric field recording of receivers for the configuration in Fig. 5 with one transmitter antenna position at $h_0 = 10$ m above the ground surface.

sources in the far field of the Earth surface, wavenumbers higher than the free space wavenumber are present with vanishing field strength in the data, leading to a limited source–receiver offset range that can be reconstructed. The data that are reconstructed in such situations are still very accurate at small offsets. This means that the monostatic and bistatic modes of operation can be retrieved from this type of measurements and interferometry procedure and opens the way for passive GPR applications by exploiting solar and extraterrestrial electromagnetic noise in the GPR bandwidth to reconstruct GPR data without reflections from the Earth surface in the data.

APPENDIX FLUX-NORMALIZED DECOMPOSITION AND COMPOSITION OPERATORS

For 3-D electromagnetic waves and fields in an acquisition configuration where depth is the preferred direction, we store the transverse electric and magnetic field components in the wave vector

$$\hat{\mathbf{f}} = (\hat{E}_1, \hat{E}_2, \hat{H}_2, -\hat{H}_1)^t \quad (20)$$

which we can write as $\hat{\mathbf{f}} = (\hat{\mathbf{f}}_1^t, \hat{\mathbf{f}}_2^t)^t$, where $\hat{\mathbf{f}}_1$ contains the two components of the electric field and $\hat{\mathbf{f}}_2$ contains the two components of the magnetic field. The vector $\hat{\mathbf{f}}$ satisfies the source free vector Maxwell equation given by

$$\partial_3 \hat{\mathbf{f}} = \hat{\mathbf{A}} \hat{\mathbf{f}} \quad (21)$$

with the system matrix $\hat{\mathbf{A}}$ given by

$$\hat{\mathbf{A}} = \begin{pmatrix} \mathbf{O} & \hat{\mathbf{A}}_{12} \\ \hat{\mathbf{A}}_{21} & \mathbf{O} \end{pmatrix} \quad (22)$$

where the antidiagonal block matrix operators are given by

$$\hat{\mathbf{A}}_{12} = \begin{pmatrix} -\zeta + \partial_1 \eta^{-1} \partial_1 & \partial_1 \eta^{-1} \partial_2 \\ \partial_2 \eta^{-1} \partial_1 & -\zeta + \partial_2 \eta^{-1} \partial_2 \end{pmatrix} \quad (23)$$

$$\hat{\mathbf{A}}_{21} = \begin{pmatrix} -\eta + \partial_2 \zeta^{-1} \partial_2 & -\partial_2 \zeta^{-1} \partial_1 \\ -\partial_1 \zeta^{-1} \partial_2 & -\eta + \partial_1 \zeta^{-1} \partial_1 \end{pmatrix}. \quad (24)$$

Note that $\hat{\mathbf{A}}$ obeys the symmetry relation

$$\hat{\mathbf{A}}^t \mathbf{N} = -\mathbf{N} \hat{\mathbf{A}} \quad (25)$$

where the property $\partial_\alpha^t = -\partial_\alpha$ is used. For the decomposition of $\hat{\mathbf{A}}$, we assume that, at the two boundaries $\partial \mathbb{D}_1$ and $\partial \mathbb{D}_m$, the medium is homogeneous, and we apply a 2-D horizontal spatial Fourier transformation defined as

$$\tilde{\mathbf{f}}(\mathbf{k}_T, x_3, \omega) = \int_{\mathbf{x}_T \in \mathbb{R}^2} \exp(j\mathbf{k}_T \cdot \mathbf{x}_T) \hat{\mathbf{f}}(\mathbf{x}, \omega) d^2 \mathbf{x}_T \quad (26)$$

where the horizontal vectors are denoted with a subscript T , such as $\mathbf{k}_T = (k_1, k_2)$. Applying this transformation to (21) gives a transformed algebraic system matrix obeying the following symmetry property in the transformed domain:

$$\tilde{\mathbf{A}}^t(-\mathbf{k}_T, x_3, \omega) \mathbf{N} = -\mathbf{N} \tilde{\mathbf{A}}(\mathbf{k}_T, x_3, \omega) \quad (27)$$

where the minus sign in the argument of the left-hand side is due to the sign change under transposition of the partial derivatives with respect to the horizontal coordinates.

Decomposition into down and up going wave field potentials is established by carrying out an eigenvalue decomposition on the system matrix $\tilde{\mathbf{A}}$ such that

$$\tilde{\mathbf{A}} = \tilde{\mathbf{L}} \tilde{\mathbf{\Gamma}} \tilde{\mathbf{L}}^{-1} \quad (28)$$

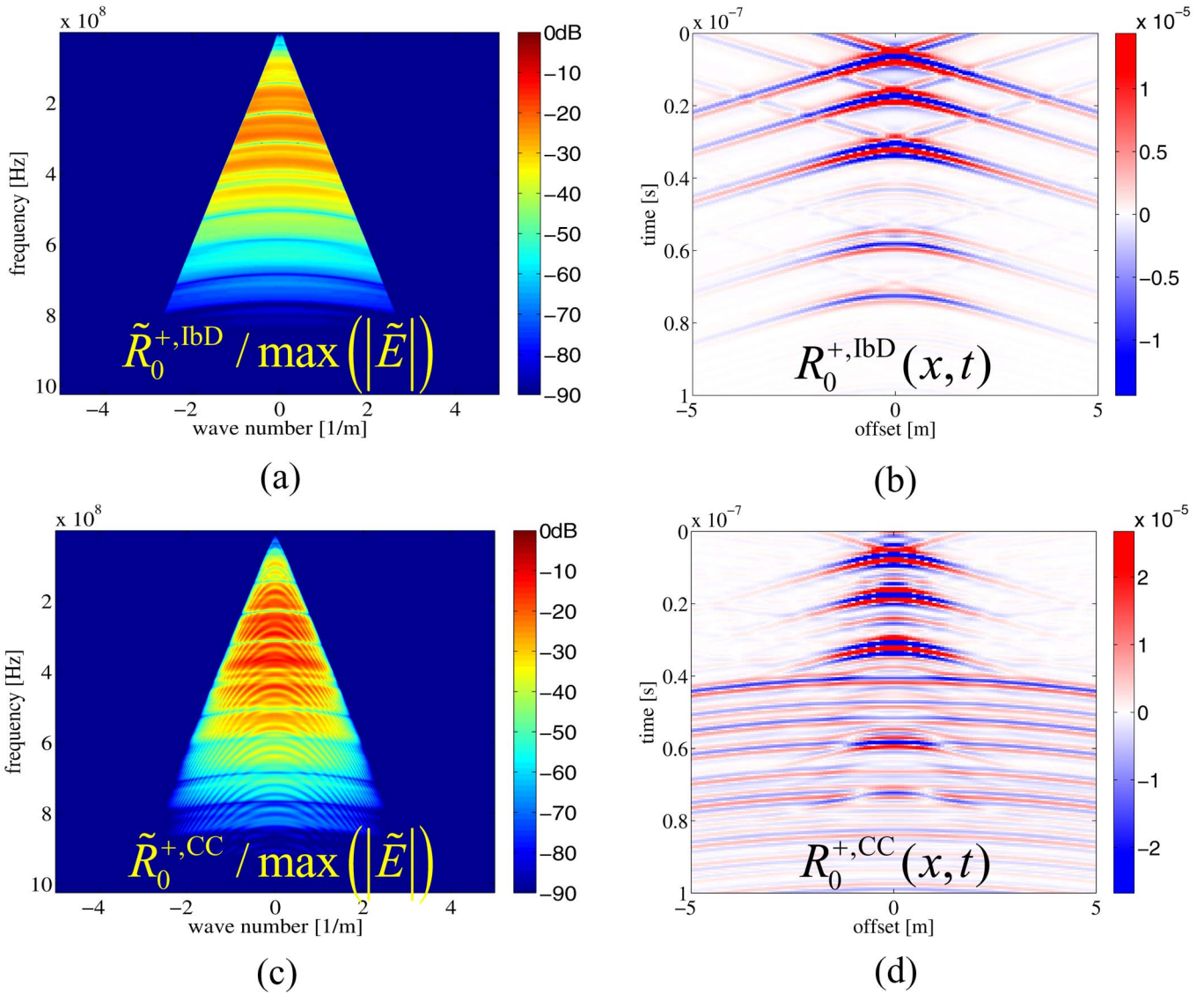


Fig. 9. Reflection responses obtained from the data shown in Fig. 8 obtained by deconvolution in the (a) wavenumber–frequency and (b) space–time domains and similar results obtained by cross correlation in the (c) wavenumber–frequency and (d) space–time domains. The wavenumber–frequency domain results are normalized by the maximum amplitude of the electric field strength.

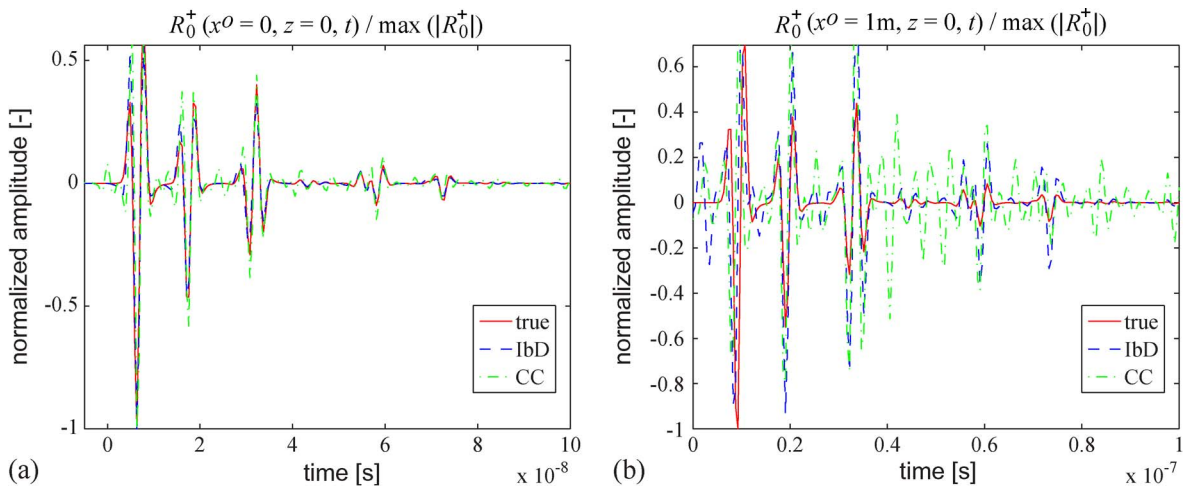


Fig. 10. Comparison of exact reflection response and the two responses obtained by the interferometry methods in the time domain at (a) zero offset $x^O = 0$ and at (b) 1-m offset $x^O = 1$ m. All reflection responses are normalized to their own maximum amplitude.

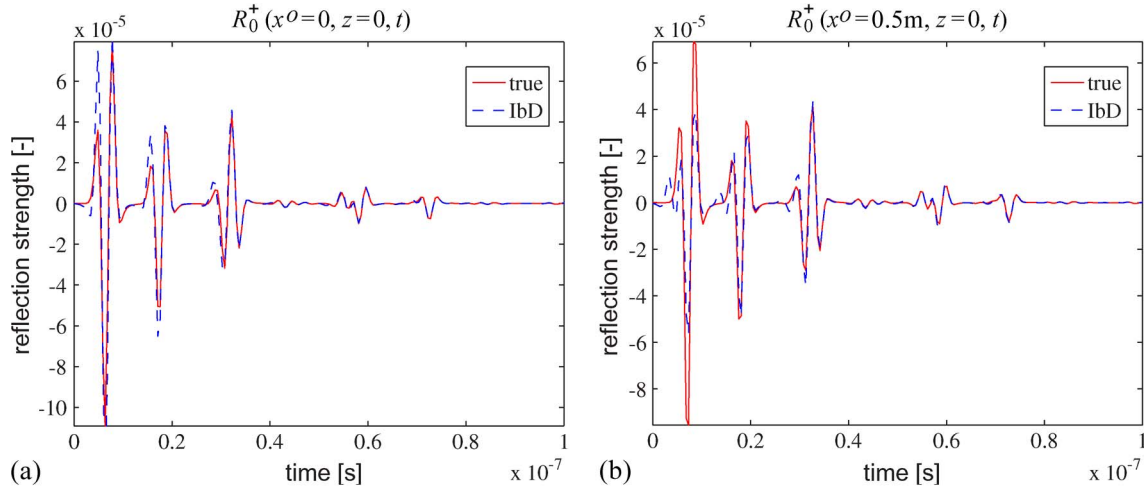


Fig. 11. True amplitude comparison of the IbD results and the exact result in the time domain at (a) zero offset $x^O = 0$ and at (b) 50-cm offset $x^O = 0.5$ m.

where $\tilde{\mathbf{L}}$ denotes the composition matrix and $\tilde{\mathbf{\Gamma}}$ is given by

$$\tilde{\mathbf{\Gamma}} = \begin{pmatrix} -\tilde{\mathbf{\Gamma}}_1 & \mathbf{O} \\ \mathbf{O} & \tilde{\mathbf{\Gamma}}_1 \end{pmatrix} \quad \tilde{\mathbf{\Gamma}}_1 = \begin{pmatrix} \tilde{\mathbf{\Gamma}} & 0 \\ 0 & \tilde{\mathbf{\Gamma}} \end{pmatrix} \quad (29)$$

with $\tilde{\mathbf{\Gamma}} = \sqrt{k_1^2 + k_2^2 + \eta\zeta}$, $\Re\{\tilde{\mathbf{\Gamma}}\} \geq 0$. Flux normalization requires $\tilde{\mathbf{L}}$ to obey the following symmetry relation:

$$\tilde{\mathbf{L}}^{-1}(\mathbf{k}_T, x_3, \omega) = -\mathbf{N}^{-1}\tilde{\mathbf{L}}^t(-\mathbf{k}_T, x_3, \omega)\mathbf{N}. \quad (30)$$

With this scaling, we obtain

$$\tilde{\mathbf{L}} = \begin{pmatrix} \tilde{\mathbf{L}}_1 & \tilde{\mathbf{L}}_2 \\ \tilde{\mathbf{L}}_2 & -\tilde{\mathbf{L}}_1 \end{pmatrix} \quad \tilde{\mathbf{L}}^{-1} = \frac{1}{2} \begin{pmatrix} \tilde{\mathbf{L}}_1^{-1} & \tilde{\mathbf{L}}_2^{-1} \\ \tilde{\mathbf{L}}_2^{-1} & -\tilde{\mathbf{L}}_1^{-1} \end{pmatrix} \quad (31)$$

where

$$\tilde{\mathbf{L}}_1 = \frac{1}{\kappa\sqrt{2}} \begin{pmatrix} jk_1\sqrt{\frac{\tilde{\mathbf{\Gamma}}}{\eta}} & -jk_2\sqrt{\frac{\tilde{\mathbf{\Gamma}}}{\zeta}} \\ jk_2\sqrt{\frac{\tilde{\mathbf{\Gamma}}}{\eta}} & jk_1\sqrt{\frac{\tilde{\mathbf{\Gamma}}}{\zeta}} \end{pmatrix} \quad (32)$$

$$\tilde{\mathbf{L}}_2 = \frac{1}{\kappa\sqrt{2}} \begin{pmatrix} jk_1\sqrt{\frac{\tilde{\mathbf{\Gamma}}}{\zeta}} & -jk_2\sqrt{\frac{\tilde{\mathbf{\Gamma}}}{\eta}} \\ jk_2\sqrt{\frac{\tilde{\mathbf{\Gamma}}}{\zeta}} & jk_1\sqrt{\frac{\tilde{\mathbf{\Gamma}}}{\eta}} \end{pmatrix} \quad (33)$$

and in view of (30), the inverse submatrices can be written in terms of the transpose submatrices as $\tilde{\mathbf{L}}_1^{-1} = -2\tilde{\mathbf{L}}_2^t$ and $\tilde{\mathbf{L}}_2^{-1} = -2\tilde{\mathbf{L}}_1^t$. Notice that, with this choice of the composition and decomposition matrices, the TE- and TM-mode reflection coefficients are obtained in the case of horizontally layered media, unlike with the choice of [28]. Using these composition and decomposition matrices, we can compose the physical fields from the flux-normalized potentials and vice versa by

$$\tilde{\mathbf{f}} = \tilde{\mathbf{L}}\tilde{\mathbf{p}}, \quad \tilde{\mathbf{p}} = \tilde{\mathbf{L}}^{-1}\tilde{\mathbf{f}} \quad (34)$$

using the expressions in (31)–(33). We can now start with (16) and substitute the expressions for $\tilde{\mathbf{p}}^\pm$ to obtain an expression for the reflection coefficient in terms of measured electric and magnetic field components in the wavenumber–frequency domain as

$$\tilde{\mathbf{R}}_0^+ = \left(\tilde{\mathbf{L}}_2^t\tilde{\mathbf{f}}_1 - \tilde{\mathbf{L}}_1^t\tilde{\mathbf{f}}_2 \right) \left(\tilde{\mathbf{L}}_2^t\tilde{\mathbf{f}}_1 + \tilde{\mathbf{L}}_1^t\tilde{\mathbf{f}}_2 \right)^{-1}. \quad (35)$$

Space-time domain results are obtained by inverse Fourier transformations.

REFERENCES

- [1] F. Scherbaum, “Seismic imaging of the site response using microearthquake recordings: Part I. method,” *Bull. Seismol. Soc. Amer.*, vol. 77, no. 6, pp. 1905–1923, Dec. 1987.
- [2] M. J. Buckingham, B. V. Berkhout, and S. A. L. Glegg, “Imaging the ocean with ambient noise,” *Nature*, vol. 356, no. 6367, pp. 327–329, Mar. 1992.
- [3] K. Wapenaar, D. Draganov, and J. Robertsson, Eds. *Seismic Interferometry: History and Present Status*. Tulsa, OK: Soc. Exploration Geophysicists, 2008. Geophysics Reprint Series (to be published).
- [4] E. Baysal, D. Kosloff, and J. Sherwood, “Reverse time migration,” *Geophysics*, vol. 48, no. 11, pp. 1514–1524, Nov. 1983.
- [5] M. Fink, “Time reversal of ultrasonic fields—Part I: Basic principles,” *IEEE Trans. Ultrason., Ferroelectr., Freq. Control*, vol. 39, no. 5, pp. 555–566, Sep. 1992.
- [6] M. Fink, “Time-reversed acoustics,” *Phys. Today*, vol. 50, no. 12, pp. 34–40, Dec. 1997.
- [7] B. Henty and D. Stancil, “Multipath-enabled super-resolution for RF and microwave communication using phase-conjugate arrays,” *Phys. Rev. Lett.*, vol. 93, no. 24, pp. 243 904-1–243 904-4, Dec. 2004. DOI: 10.1103/PhysRevLett.93.243 904.
- [8] D. Liu, J. Krolik, and L. Carin, “Electromagnetic target detection in uncertain media: Time-reversal and minimum-variance algorithms,” *IEEE Trans. Geosci. Remote Sens.*, vol. 45, no. 4, pp. 934–944, Apr. 2007.
- [9] M. E. Yavuz and F. L. Teixeira, “Space–frequency ultrawideband time-reversal imaging,” *IEEE Trans. Geosci. Remote Sens.*, vol. 46, no. 4, pp. 1115–1124, Apr. 2008.
- [10] R. Streich and J. van der Kruk, “Accurate imaging of multicomponent GPR data based on exact radiation patterns,” *IEEE Trans. Geosci. Remote Sens.*, vol. 45, no. 1, pp. 93–103, Jan. 2007.
- [11] E. Slob, D. Draganov, and K. Wapenaar, “GPR without a source,” in *Proc. 11th Int. Conf. GPR*, 2006, p. Ant.6.
- [12] E. Slob, D. Draganov, and K. Wapenaar, “Interferometric electromagnetic Green’s functions representations using propagation invariants,” *Geoph. J. Int.*, vol. 169, no. 1, pp. 60–80, 2007. DOI:10.1111/j.1365-246X.2006.03 296.x.
- [13] E. Slob and K. Wapenaar, “GPR without a source: Cross-correlation and cross-convolution methods,” *IEEE Trans. Geosci. Remote Sens.*, vol. 45, no. 8, pp. 2501–2510, Aug. 2007.
- [14] E. Slob and K. Wapenaar, “Electromagnetic Green’s functions retrieval by cross-correlation and cross-convolution in media with losses,” *Geophys. Res. Lett.*, vol. 34, no. 5, p. L05 307, 2007. DOI:10.1029/2006GL029 097.
- [15] L. B. Liu and K. He, “Wave interferometry applied to borehole radar: Virtual multioffset reflection profiling,” *IEEE Trans. Geosci. Remote Sens.*, vol. 45, no. 8, pp. 2554–2559, Aug. 2007.
- [16] R. Snieder, “Retrieving the Green’s function of the diffusion equation from the response to a random forcing,” *Phys. Rev. E, Stat. Phys. Plasmas Fluids Relat. Interdiscip. Top.*, vol. 74, no. 4, pp. 046 620-1–046 620-4, Oct. 2006. DOI:10.1103/PhysRevE.74.046 620.

- [17] R. Snieder, "Extracting the Green's function of attenuating heterogeneous acoustic media from uncorrelated waves," *J. Acoust. Soc. Amer.*, vol. 121, no. 5, pp. 2637–2643, May 2007.
- [18] R. L. Weaver, "Ward identities and the retrieval of Green's functions in the correlations of a diffuse field," *Wave Motion*, vol. 45, pp. 596–604, 2008.
- [19] K. Wapenaar and E. Slob, "Unified Green's function retrieval by cross correlation," *Phys. Rev. Lett.*, vol. 97, no. 23, pp. 234 301-1–234 301-4, Dec. 2006. DOI:10.1103/PhysRevLett.97.234 301.
- [20] R. Snieder, K. Wapenaar, and U. Wegler, "Unified Green's function retrieval by cross-correlation; connection with energy principles," *Phys. Rev. E, Stat. Phys. Plasmas Fluids Relat. Interdiscip. Top.*, vol. 75, no. 3, pp. 036 103-1–036 103-14, Mar. 2007.
- [21] K. Wapenaar, E. Slob, and R. Snieder, "Seismic and electromagnetic controlled-source interferometry in dissipative media," *Geophys. Prospect.*, vol. 56, no. 3, pp. 419–434, May 2008.
- [22] D. Riley and J. Claerbout, "2-D multiple reflections," *Geophysics*, vol. 41, no. 4, pp. 592–620, Aug. 1976.
- [23] R. Snieder, J. Sheiman, and R. Calvert, "Equivalence of the virtual-source method and wave-field deconvolution in seismic interferometry," *Phys. Rev. E, Stat. Phys. Plasmas Fluids Relat. Interdiscip. Top.*, vol. 73, no. 6, pp. 066 620-1–066 620-9, Jun. 2006. DOI:10.1103/PhysRevE.73.066 620.
- [24] J. van der Kruk and E. C. Slob, "Reduction of reflections from above surface objects in GPR data," *J. Appl. Geophys.*, vol. 55, no. 3/4, pp. 271–278, Mar. 2004.
- [25] A. Ruffell, "Under-water scene investigation using ground penetrating radar (GPR) in the search for a sunken jet ski, Northern Ireland," *Sci. Justice*, vol. 46, no. 4, pp. 221–230, Oct.–Dec. 2006.
- [26] M. Frijlink, "Seismic redatuming with transmission loss correction in complex media," Ph.D. dissertation, Delft Univ. Technol., Delft, The Netherlands, 2007.
- [27] C. P. A. Wapenaar and J. L. T. Grimbergen, "Reciprocity theorems for one-way wavefields," *Geophys. J. Int.*, vol. 127, no. 1, pp. 169–177, 1996.
- [28] B. Ursin, "Review of elastic and electromagnetic wave propagation in horizontally layered media," *Geophysics*, vol. 48, no. 8, pp. 1063–1081, Aug. 1983.
- [29] A. G. Yarovoy, R. V. deJongh, and L. P. Ligthart, "Ultra-wideband sensor for electromagnetic field measurements in time domain," *Electron. Lett.*, vol. 36, no. 20, pp. 1115–1124, Sep. 2000.
- [30] A. G. Yarovoy, T. G. Savelyev, P. J. Aubry, P. E. Lys, and L. P. Ligthart, "UWB array-based sensor for near-field imaging," *IEEE Trans. Microw. Theory Tech.*, vol. 55, no. 6, pt. 2, pp. 1288–1295, Jun. 2007.
- [31] E. Holvik and L. Amundsen, "Elimination of the overburden response from multicomponent source and receiver seismic data, with source designation and decomposition in PP-, PS-, SP- and SS-wave responses," *Geophysics*, vol. 70, no. 2, pp. SI11–SI21, 2005.
- [32] A. Berkhout, *Seismic Migration, Imaging of Acoustic Energy by Wavefield Extrapolation*. Amsterdam, The Netherlands: Elsevier, 1982.
- [33] K. Wapenaar and D. Verschuur, "Processing of ocean bottom data," in *The Dolphin Project*, vol. I. Delft, The Netherlands: Delft Univ. Technol., 1996, pp. 6.1–6.26.
- [34] A. Berkhout and D. Verschuur, "Transformation of multiples into primaries," in *Proc. Expanded Abstracts 73rd Annu. Int. Meeting Soc. Expl. Geophys.*, 2003, pp. 1925–1928.
- [35] G. Schuster and M. Zhou, "A theoretical overview of model-based and correlation-based redatuming methods," *Geophysics*, vol. 71, no. 4, pp. SI 103–SI 110, 2006.
- [36] A. Bakulin and R. Calvert, "The virtual source method: Theory and case study," *Geophysics*, vol. 71, no. 4, pp. SI 139–SI 150, Jul./Aug. 2006.



Evert Slob received the M.Sc. degree in mining and petroleum engineering and the Ph.D. degree (*cum laude*) in applied sciences from Delft University of Technology (TU Delft), Delft, The Netherlands, in 1989 and 1994, respectively.

Since 1995, he has been with TU Delft, where he was with the Department of Applied Earth Sciences and is currently an Associate Professor with the Department of Geotechnique. He is an Associate Editor on ground-penetrating radar (GPR) and electromagnetic rock properties for the journal *Geophysics* (Society of Exploration Geophysicists) and on GPR for *Near Surface Geophysics* (European Association of Geoscientists and Engineers). He was Guest Editor for eight special journal issues on GPR and hydrogeophysics. He published 40 journal papers on these subjects. His current research interests are electromagnetic (EM) interferometry, hydrogeophysics, advanced imaging and inversion techniques, heterogeneity determination, and soil characterization including the study of fundamental relations between geological and EM and electrokinetic properties of soil and rocks, and their scale dependence.

Dr. Slob was the General Chair of the 10th International Conference on GPR in 2004 and organized three international workshops.